Carbon 246 (2026) 120934

Contents lists available at ScienceDirect

Carbon

journal homepage: www.elsevier.com/locate/carbon

Anisotropy-driven double corrugation: Coexistence of one- and two-dimensional wave patterns in epitaxial graphene on iridium

Deborah Perco [a], Monica Pozzo [b,c], Marco Bianchi [d,e], Paolo Lacovig [d], Francesco Sammartino [a], Philip Hofmann [e], Silvano Lizzit [d], Dario Alfè [f,g], Alessandro Baraldi [a,d,*]

[a] Department of Physics, University of Trieste, via Valerio 2, 34127, Trieste, Italy
[b] Faculty of Technological & Innovation Sciences, Universitas Mercatorum, Piazza Mattei 10, 00186, Rome, Italy
[c] Institute for Materials Discovery, UCL East, Marshgate Building, 7 Siding Street, Stratford, London, E20 2AE, United Kingdom
[d] Elettra - Sincrotrone Trieste, S.S. 14 Km 163.5 in AREA Science Park, 34149, Basovizza, Trieste, Italy
[e] Department of Physics and Astronomy, Interdisciplinary Nanoscience Centre (iNANO), Aarhus University, 8000, Aarhus, Denmark
[f] Department of Earth Sciences and London Centre for Nanotechnology, University College London, Gower Street, London, WC1E 6BT, United Kingdom
[g] Dipartimento di Fisica Ettore Pancini, Università di Napoli Federico II, Monte S. Angelo, 80126, Napoli, Italy

ARTICLE INFO

Keywords:
Graphene
Epitaxial graphene
Ripples
Corrugation
Curvature
Wave pattern
Iridium

ABSTRACT

Tailoring the electronic properties of graphene is crucial for a variety of applications. In this study, we investigate the graphene growth on the high Miller-index, anisotropic Ir(311) surface, where it self-organizes into one-dimensional ripples accompanied by a short-wavelength, two-dimensional wave pattern that is spatially confined between them. By employing a combination of spectroscopy- and microscopy-based techniques, we show that carbon atoms on the ripples interact weakly with the substrate, whereas those in the flatter region between two ripples experience stronger interaction with iridium atoms, leading to a partial rehybridization of carbon orbitals towards sp^3 character. Complementary density functional theory calculations identify at least three distinct families of non-equivalent carbon atoms within the graphene layer and reveal that atoms on ripples are subjected to compressive strain. Since both compressive strain and corrugation are key factors in influencing graphene's chemical reactivity, the coexistence of two different wave pattern on graphene/Ir(311) system points to a region-specific reactivity. This spatial modulation of properties offers exciting potential for the design of bifunctional catalysts, particularly for hydrogen storage applications and for advanced materials in spintronic.

1. Introduction

Since its initial isolation via mechanical exfoliation, graphene has emerged as a promising material for applications in various fields, including electronics and sensing, due to its unique properties, such as a large surface area, high thermal stability, exceptional mechanical strength, and excellent electron mobility [1–4]. Graphene has also been widely explored in catalysis, both as a support and as a catalyst itself [5–7]. However, pristine graphene in its ideal form, due to its stable, delocalized π-electron system, is considered chemically inert but it can be activated or functionalized for applications in catalysis. To achieve this, defects, strain, and doping atoms have been introduced to strengthen the interaction between graphene and catalytic species, thereby improving adsorption stability [8,9]. For instance, Zhou et al. demonstrated that the adsorption energy of gold nanoclusters increases on strained graphene [10], while nitrogen-doped graphene has been shown to act as an effective metal-free catalyst for the oxygen reduction reaction [11–13].

Another approach to modify the properties of graphene while enabling high-quality synthesis is its growth on different metallic and non metallic substrates [14,15]. It is known, for example, that the interaction of graphene with Cu depends on both crystallographic orientation and oxidation of the surface [16]. For example, Burton et al. identified Cu(168) as an ideal surface for high-quality growth and subsequent transfer of graphene [17]. On the other hand, depending on the lattice mismatch and the degree of hybridization between the carbon lattice and the substrate, graphene can adopt distinct structural configurations, ranging from a quasi-freestanding form - such as on Pt(111)

* Corresponding author. Department of Physics, University of Trieste, via Valerio 2, 34127, Trieste, Italy.
E-mail address: alessandro.baraldi@elettra.eu (A. Baraldi).

https://doi.org/10.1016/j.carbon.2025.120934
Received 8 June 2025; Received in revised form 5 September 2025; Accepted 10 October 2025
Available online 13 October 2025

and Ir(111) [18–21] - to highly corrugated geometries, as observed on Re(0001) [22], Rh(111) [23] and Ru(0001) [24,25]. These graphene-metal interfaces can also serve as templates for the growth of two-dimensional periodic arrays of atoms, molecules and nanoparticles [26–34]. Among substrates that lack C_{3v} symmetry, Ir(100) is particularly notable, as graphene grown on this surface exhibits two distinct and spatially separated structures, as determined by low-energy electron microscopy and theoretical calculations [35,36]. In most regions, the carbon layer remains nearly flat and interacts weakly with the Ir atoms. However, in certain areas, periodic two-dimensional ripples form, where small rows of carbon atoms exhibit strong interactions with the substrate [37]. This strong interaction is reflected in the C 1s core-level spectrum, where an additional component—accounting for approximately 2.1 % of the total spectral weight—appears at a higher binding energy (BE) (+0.90 eV) compared to the peak associated with weakly interacting carbon atoms, a feature commonly observed in graphene-metal systems with strong substrate interactions [38,39].

Among the various metal substrates, anisotropic and high Miller-index surfaces offer an alternative strategy for producing unique templates. Their periodic arrays of atomic steps provide an excellent platform for inducing one-dimensional modulations in graphene. On Cu (410)-O, for example, graphene forms a quasi-one-dimensional superlattice with a periodicity matching that of the substrate steps (7.4 Å), similar to observations on Cu(311) and Cu(210) [40]. On Fe(110), strong carbon-iron interactions give rise to one-dimensional wave-like structures with a periodicity of 4 nm [41]. Conversely, graphene growth on Ir(332) modifies the original step structure, resulting in the formation of wider (111) terraces and step bunching [42,43]. On Ir(110), graphene adopts a wave-like pattern with a nanometer-scale wavelength and an apparent corrugation of only 0.4 Å [44]. However, in all these graphene-metal systems, the formation of one- or two-dimensional patterns occurs either on different metal substrates or in different but macroscopically separated regions of the same substrate.

In this work, we report on the growth of graphene on the vicinal Ir (311) surface, where the carbon layer simultaneously exhibits both a long-wavelength one-dimensional corrugation and a short-wavelength two-dimensional pattern, spatially confined between the ripples formed by the first morphology. Using a combination of spectroscopy- and microscopy-based experimental techniques, complemented by density functional theory (DFT) calculations, we demonstrate that graphene can be synthesized on this surface, forming periodic one-dimensional ripples where carbon atoms interact weakly with the substrate (maximum C–Ir distances of 3.41 Å). In addition, we identify flatter regions between the ripples where carbon atoms chemisorb onto surface Ir atoms. Within these flatter regions, we reveal an additional modulation in the C-substrate distance, with C–Ir distances in the range 2.12–2.7 Å, attributed to alternating stronger and weaker interactions between carbon and iridium atoms—particularly where carbon atoms are positioned directly above second-layer Ir atoms of this highly open surface. The formation of these combined one- and two-dimensional corrugation patterns introduces a novel template for region-defined catalysis, as different graphene curvatures are known to strongly influence adsorption, dissociation, and reactivity of graphene [45–47].

2. Methods

2.1. Experimental methods

Low Energy Electron Diffraction (LEED) and Spot-Profile Analysis LEED (SPA-LEED) images were acquired in an Ultra High Vacuum (UHV) chamber at the Nanoscale Materials Laboratory at Elettra – Sincrotrone Trieste. The Omicron SPA-LEED system allows the measurement of the diffraction spots line shape, with a transfer width of the instrument which is better than 700 Å at electron kinetic energy of 115 eV. The base pressure was always below 2×10^{-10} mbar. High Resolution Core Level Spectroscopy (HR-CLS) experiments were carried out at the SuperESCA beamline of the Elettra synchrotron radiation facility. The measurement chamber is equipped with a SPECS Phoibos 150 electron energy analyzer, provided with a delay line detector developed in house, LEED and mass spectrometer. The overall energy resolution was better than 80 meV for the chosen photon energies and acquisition parameters. The HR-CLS spectra were acquired by tuning the photon energy such to have a photoelectron kinetic energy of about 100 eV for the different core levels, enhancing surface sensitivity.

Scanning Tunneling Microscopy (STM) and ARPES (Angle Resolved Photoemission Spectroscopy) measurements were performed at the SGM3 end-station of the synchrotron radiation facility ASTRID2 in Aarhus (DK), equipped with a home-built Aarhus STM at room temperature, a Phoibos 150 spectrometer, a LEED unit and mass spectrometer [48]. ARPES data were collected at room temperature using different photon energies between 44 eV and 110 eV with a combined energy and angular resolution better than 30 meV and 0.2° respectively. The sample was prepared in similar way in all the experimental set-ups, always crosschecking for consistency either the LEED pattern or the characteristics Ir core levels.

Ir(311) crystal was cleaned by repeated cycles of Ar^+ sputtering and annealing up to 1373 K. All the core level spectra were analysed using a Doniach-Šunjič function (DS) convoluted with a Gaussian distribution. The DS profile combines a Lorentzian width L, which is related to the finite core-hole lifetime, with the Anderson singularity index, which reflects the occurrence of electron-hole pair excitations near the Fermi level. The Gaussian width G accounts for phonon broadening, instrumental resolution, and any inhomogeneous broadening. The background was assumed to be linear. The BEs scale was calibrated with respect to the Fermi energy, which was measured under the same experimental conditions on the very same sample.

2.2. Theoretical methods

The DFT calculations were performed as implemented in the Vienna Ab-initio Simulation Package (VASP) code [49]. The system was described with a slab composed of 8 layers of Ir, with a layer of graphene placed on top (see below for details). The bottom five layers of Ir were kept frozen at their bulk geometry, with a lattice parameter of 2.74 Å, and the rest of the system was fully relaxed using the rev-vdwDF2 functional [50] until the largest residual force was less than 0.015 eV/Å. We employed the projector augmented method (PAW) [51,52] using PBE potentials [53]. The plane wave cutoff was set to 400 eV, and the relaxations were performed by sampling the Brillouin zone using the Γ point only.

Core level BEs are obtained as the difference in energy from two calculations. The first is a standard calculation, and the second is a calculation in which a core electron is removed from an atom and placed in valence. This can be achieved by creating a new pseudo potential for the atom with the core hole and adding one electron to the total number of valence electrons. In the PAW formalism employed in VASP this is done during the calculation, without the need to explicitly generate a separate PAW for the atom with the hole in the core. In both calculations the total charge density is driven to self-consistency, thereby considering the relaxation of the valence electrons around the hole. The other core electrons are kept frozen, and so their screening is neglected. This is commonly known as the 'final state' approximation. The absolute values of the core level BEs obtained in these calculations cannot be related to measurable quantities, but differences in core level BEs can usually be obtained with accuracies of a few tens of meV. In order to align the measured and computed core level BEs we used a single offset parameter. Considering Ir $4f_{7/2}$ core level as example, the offset parameter has been chosen in a way that the theoretically computed core level BEs for bulk Ir atoms were aligned with the bulk peak in the core level spectrum of iridium, located at 60.84 eV.

3. Results and discussion

3.1. Structural characterization

Ir(311) is an open surface composed of two-atom-wide (111) terraces separated by monoatomic (100) steps, as illustrated in Fig. 1(a). The LEED pattern shown in Fig. 1(b) indicates that the surface does not undergo any reconstruction, in contrast for example to Pt(311) where a (1 × 2) missing-row reconstruction is observed [54].

The presence of an oblique unit cell is evidenced by the reciprocal unit vectors, labelled as $\vec{Ir}_1$* and $\vec{Ir}_2$*. The norm ratio of these vectors is 1.69 ± 0.04, and the angle between them is 73.3° ± 0.8°, in close agreement with the corresponding expected values of 1.73 and 73.2° respectively.

A monolayer of graphene was grown via the thermal decomposition of C_2H_4. The growth process involved annealing cycles, while exposing the Ir surface to ethylene at successively increasing pressures. For each cycle the crystal was maintained at the lower temperature (550 K) for 120 s to facilitate ethylene adsorption, then the temperature was gradually increased up to 1373 K to promote molecular decomposition and carbon surface diffusion for graphene formation, as for Ir(111) [55]. For the first 4 cycles the pressure was set to 5×10^{-8} mbar, then increased to 3×10^{-7} mbar for the final 3 cycles, for a total of seven cycles.

Following this procedure, upon cooling the sample to 300 K, additional diffraction spots appeared in the LEED pattern. The characteristic hexagonal diffraction pattern of graphene, confirming its symmetry, is highlighted by the two reciprocal lattice vectors, $\vec{G}_1$* and $\vec{G}_2$* that exhibit equal magnitudes, with an angle of approximately 60°, as expected for graphene (see Fig. 1(c)). Notably, the direction of $\vec{G}_1$* is aligned with $\vec{Ir}_1$*, indicating that in real space, one of the graphene unit cell vectors is oriented along the $[01\bar{1}]$, which corresponds to the direction of the shortest vector of the Ir(311) primitive cell. This alignment is further validated by LEED pattern simulations performed using *ProLEED Studio* software, as shown in Fig. 1(d) [56].

A comparison between the simulated and experimentally measured electron diffraction patterns reveals additional diffraction spots. The presence of these extra spots, as revealed by the SPA-LEED image shown in Fig. 1(e), suggests the formation of two distinct superstructures, whose unit cell vectors are denoted as $\vec{M}_1$* and $\vec{M}_2$*, and $\vec{P}_1$* and $\vec{P}_2$*, respectively. The ratio between their moduli is 1.40 ± 0.1 and 1.02 ± 0.1, respectively. The angle between $\vec{M}_1$* and $\vec{M}_2$* is 93° ± 2°, while the angle between $\vec{P}_1$* and $\vec{P}_2$* is 41° ± 1°. It is important to note that $\vec{M}_1$* is aligned with $\vec{Ir}_1$* with the ratio between their moduli being 0.13 ± 0.02. The large value of the uncertainty in this ratio is caused by the broadening of the diffraction spots. By superimposing an ideal graphene lattice onto the Ir(311) surface (see Fig. 1(f)), we can observe that (i) along the $[01\bar{1}]$ direction, 10 graphene unit cells correspond to 9 Ir cells, similarly to what is observed for Ir(111) [39], and (ii) the lattice matching along the direction orthogonal to $[01\bar{1}]$, defined by the M_1 vector, is achieved after 7 Ir periodicities, in reasonable agreement with the experimental results. The second periodicity, related to $\vec{P}_1$* and $\vec{P}_2$* vectors, however, is more difficult to be identified at a first glance.

To gain further insight into the dimensions and symmetry of the graphene/Ir unit cell, we acquired STM topographs. As shown in Fig. 2

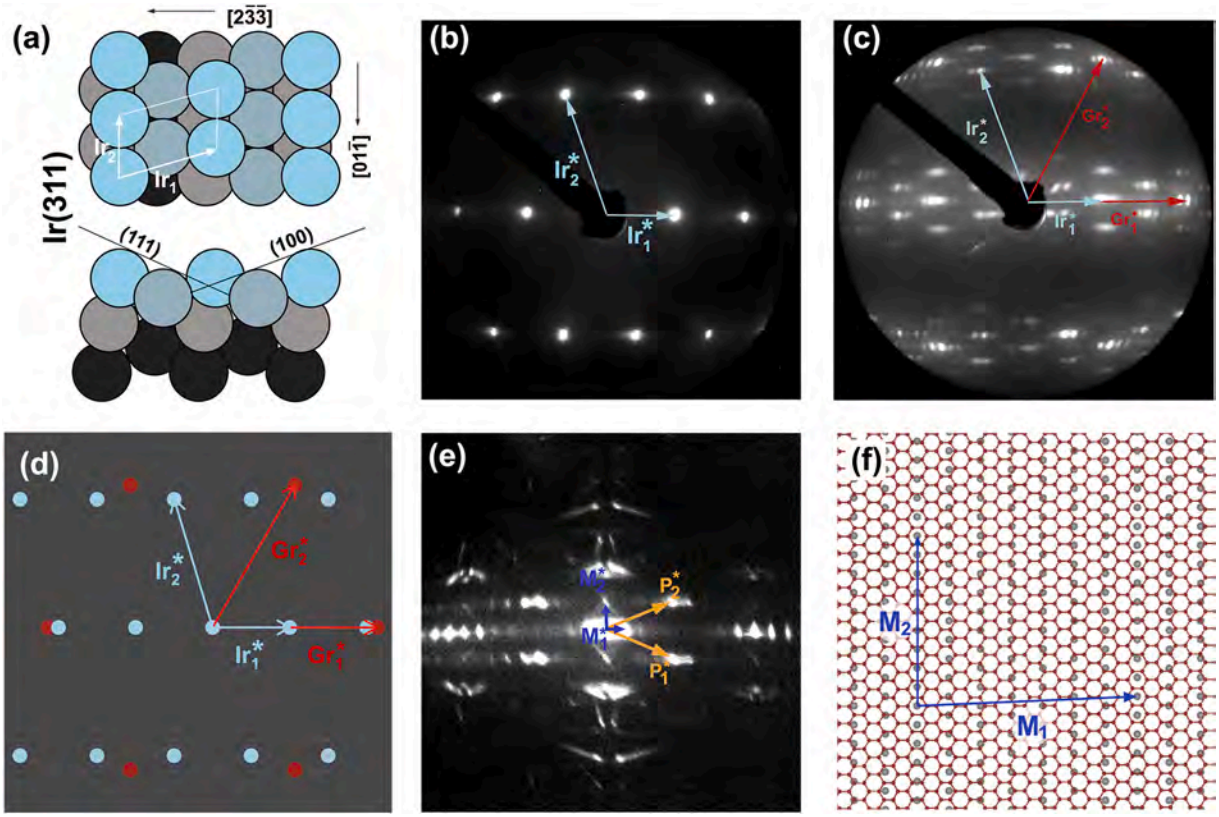

Fig. 1. Structural model and electron diffraction patterns of graphene/Ir(311). (a) Structural model of Ir(311). (b) LEED pattern of Ir(311) surface acquired at E = 158 eV. (c) LEED pattern of graphene/Ir(311) acquired at E = 120 eV. (d) Simulated LEED pattern of graphene/Ir(311). Red circles and vectors represent graphene lattice; Light blue circles and vectors are associated to Ir lattice. (e) SPA-LEED pattern of graphene/Ir(311) acquired at E = 85.5 eV $\vec{M}_1$* and $\vec{M}_2$* are depicted in blue, while $\vec{P}_1$* and $\vec{P}_2$* in orange. (f) Top view of the structural model with superposition of an ideal Ir(311) surface (first-layer Ir atoms in grey) and a graphene monolayer (red balls) oriented according to LEED findings. The $\vec{M}_1$ and $\vec{M}_2$ real space vectors are shown in blue. (For interpretation of the references to color in this figure legend, the reader is referred to the Web version of this article.)

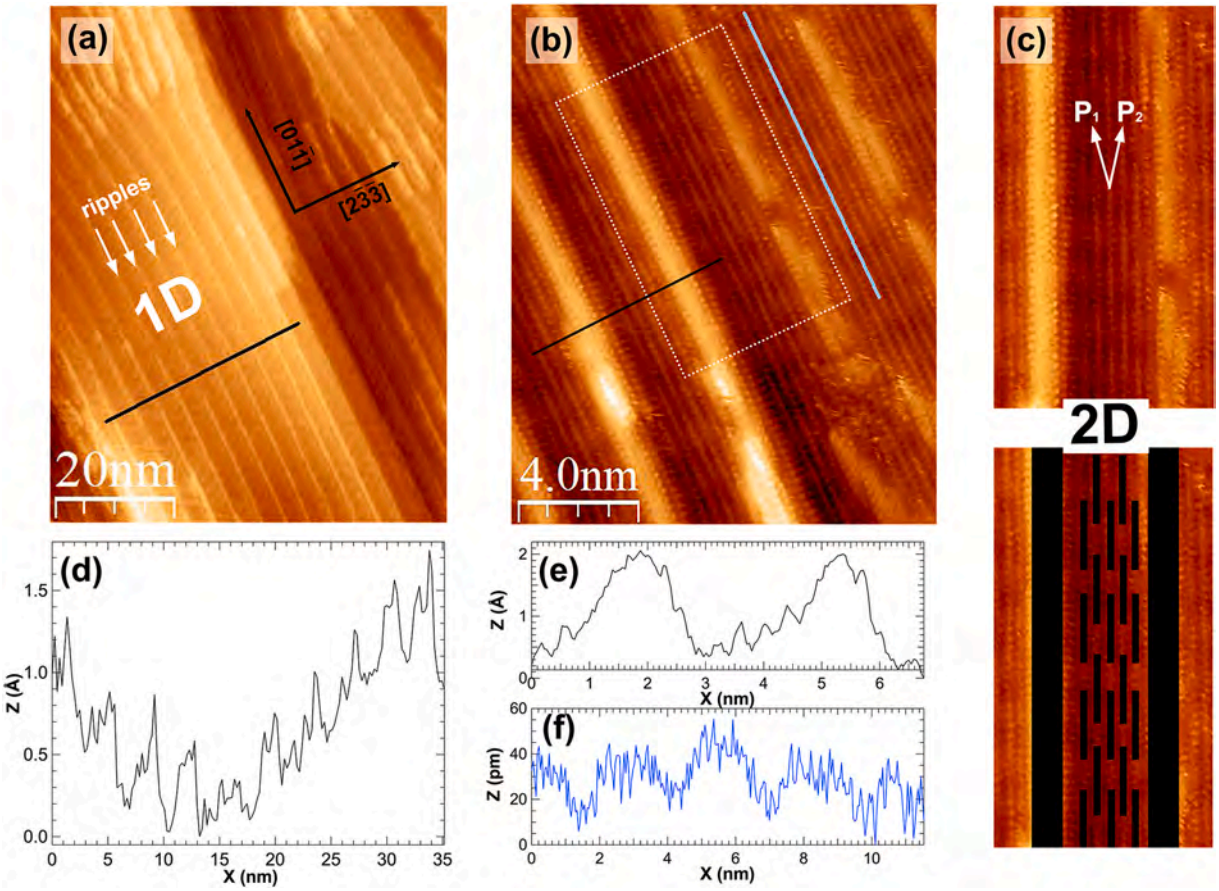

Fig. 2. STM topographs and line profiles. (a) STM image (70 × 91 nm^2) of large Ir terraces covered with graphene. (b) STM image (13 × 17 nm^2) with higher resolution. (c) Enlarged region defined by the dashed rectangle shown in panel (b), where the vectors P_1 and P_2, corresponding to the reciprocal lattice vectors $\vec{P}_1$* and $\vec{P}_2$* shown in Fig. 1(e), are reported. The lower part of the panel serves as a visual guide to highlight the two-dimensional corrugation present between the one-dimensional ripples. (d) Line profile of the STM image in panel (a) along the black line. (e) Line profile of the STM image in panel (b) along the black line. (f) Line profile of the STM image in panel (b) along the blue line. Tunneling parameters are (a) $V_t = -42.1$ mV, $I_t = -330$ pA. (b) $V_t = -50.4$ mV, $I_t = 190$ pA. (For interpretation of the references to color in this figure legend, the reader is referred to the Web version of this article.)

(a), large, flat terraces of Ir(311) are uniformly covered with graphene, exhibiting an ordered and periodic series of ripples oriented along the [01$\bar{1}$] direction. A zoom on a flat terrace, shown in Fig. 2(b), reveals the distinctive periodic structure formed by graphene between the main ripples, characterized by alternating rows of dark and bright features running parallel to the ripples.

Line profiles taken perpendicularly to the ripples provide measurements of their average apparent height and periodicity, which are 1.47 ± 0.34 Å and 33.73 ± 1.09 Å, respectively (see Fig. 2(c) and (d)). In the regions between the ripples, the bright features exhibit a periodicity of 2.71 ± 0.02 Å along [01$\bar{1}$] direction, corresponding to the atomic spacing of Ir in the (111) terraces of Ir(311). While the hexagonal graphene lattice is clearly visible on the ripples (see Fig. S1 in Supplementary Material), the flatter regions in between are likely dominated by electronic effects arising from graphene-substrate interactions. This observation suggests that the main corrugation can be associated with weakly interacting C atoms, whereas in other regions, the graphene-substrate interaction is stronger. The line profile along the [01$\bar{1}$] direction (Fig. 2(e)) reveals an additional atomic buckling with an average corrugation amplitude of 0.3 Å. The highest parts of the corrugation along the [01$\bar{1}$] direction are found in a running bond arrangement as can be seen in Fig. 2(b). This characteristic periodic pattern between the ripples gives rise to the $\vec{P}_1$* and $\vec{P}_2$* vectors in Fig. 1(e). The real space vectors, $\vec{P}_1$ and $\vec{P}_2$, derived from the STM image of Fig. 2(b), present a modulus equal to 14.2 ± 0.3 Å, while the angle between them is 37.5° ± 2°, comparable within the error bars with the results obtained from SPA-LEED imaging.

To investigate the properties of the non-equivalent carbon atoms in graphene, which give rise to the observed 1D and 2D corrugations, we performed DFT calculations. On the basis of STM and LEED results, we chose a unit cell that minimizes strain in the graphene lattice. The shortest vector of the supercell is aligned along the [01$\bar{1}$] crystallographic direction and has a length of 24.66 Å, corresponding to 9 Ir interatomic spacings. The second vector is tilted by 2.45° relative to the perpendicular direction and has a length of 31.94 Å. The ratio between Ir_1 and the latter vector of the supercell is 0.15, consistent with the ratio between M_1* and Ir_1* derived from LEED and SPA-LEED data analysis. The graphene lattice parameters deviate only slightly from those of free-standing graphene: 2.458 Å along the [2$\bar{3}\bar{3}$] direction, representing a 0.18 % contraction, and 2.466 Å along the [01$\bar{1}$] direction, corresponding to a 0.12 % elongation. Notably, no initial corrugation was imposed on the graphene structure in the original DFT input cell.

Upon relaxation, the buckling of carbon atoms gives rise to the formation of ripples at the edges of the supercell, which closely resembles those observed in STM. The DFT structural model and calculated C–Ir distances in the supercell are displayed in Fig. 3. In this figure, small circles stand for C atoms, while Ir atoms are displayed with bigger circles. Specifically, first layer Ir atoms are colored in light grey, while second layer Ir atoms are colored in dark grey. The maximum C–Ir

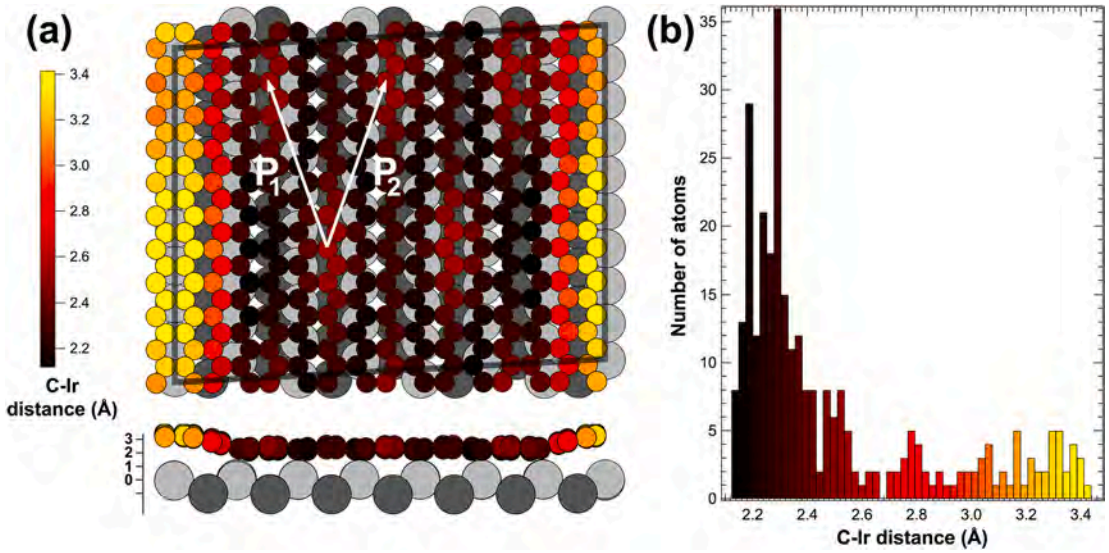

Fig. 3. DFT calculated C–Ir distances. (a) Top and side views of the DFT structural model of graphene/Ir(311). Color scale reflects the separation between C atoms and the Ir substrate beneath. P_1 and P_2 vectors are shown with white arrows. (b) Histogram of the carbon atomic population as a function of C–Ir distance. (For interpretation of the references to color in this figure legend, the reader is referred to the Web version of this article.)

distance of carbon atoms on ripples is 3.41 Å, a value close to the C–Ir height in graphene/Ir(111) [57], for a maximum corrugation of 1.29 Å.

A closer inspection of the relaxed cell shows, besides the ripples, also the presence of a 2D corrugation. This 2D corrugation is highlighted by $\vec{P}_1$ and $\vec{P}_2$ vectors in the flatter part of the cell, in between two ripples. The average periodicity of this wave pattern along the $[2\bar{3}\bar{3}]$ direction is 8.64 Å with a vertical displacement of 0.43 Å. Along the $[01\bar{1}]$ direction of the cell, the graphene lattice parameter remains almost unchanged with respect to the unrelaxed slab. However, another corrugation is present. C atoms placed on top of second-layer Ir atoms are in turn vertically displaced by 0.43 Å and this wrinkling presents the same periodicity of the supercell in the $[01\bar{1}]$ direction. These two corrugations give rise to the running bond bright-dark spots pattern which was imaged by STM (Fig. 2(b)). The modulus of the P_1 and P_2 vectors, shown in Fig. 3(a), that define these corrugations and the angle between them, i.e. 14.06 Å and 39.2°, are consistent with the ones of $\vec{P}_1$* and $\vec{P}_2$* vectors revealed by SPA-LEED analysis and the corresponding real space vector derived from STM.

3.2. Chemical and electronic properties of the Gr/Ir interface

HR-CLS measurements confirm the presence of non-equivalent carbon atoms on the surface. The C 1s core level spectrum, shown in Fig. 4 (a), initially appears to consist of two peaks. However, fitting the spectrum using only two components resulted in a poor-quality fit (blue line in Fig. 4(a)). In contrast, incorporating a third component with the same Lorentzian width and singularity index significantly improves the

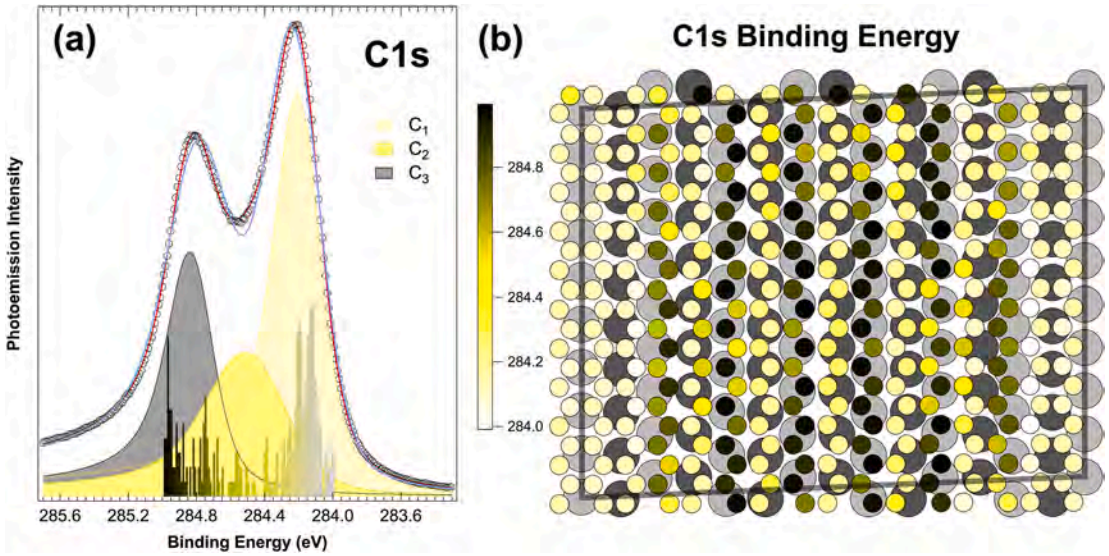

Fig. 4. C 1s core level spectrum and DFT computed C core levels distribution. (a) C1s core level spectrum of graphene/Ir(311) measured at normal emission and $h\upsilon = 400$ eV (empty circles). Red line represents the fit obtained with three components, while the blue one identifies the fit done using two components. Colored lines are used to identify the three carbon atom families used in the approximation. The superimposed histograms display the C atomic population as a function of the DFT calculated core-levels. (b) Structural model of the supercell where the color scale used for non-equivalent C atoms reflects the DFT-calculated C 1s core electron BEs. First- and second-layer Ir atoms are shown in light and dark grey, respectively. (For interpretation of the references to color in this figure legend, the reader is referred to the Web version of this article.)

fit, accurately reproducing the experimental spectrum (red line in Fig. 4 (a)). The BEs of the three identified components are 284.19 ± 0.03 eV, 284.48 ± 0.03 eV, and 284.81 ± 0.03 eV. We would like to point out that fitting with three components constitutes a simplified picture as each inequivalent carbon atom has its own core level, as supported by DFT-calculated core electron BEs and illustrated in Fig. 4(b). In this figure, carbon atoms exhibiting different C 1s BEs are color-coded accordingly. This differentiation appears also in the histogram shown in the lower part of Fig. 4(a) where, besides the peaks at high and low BEs, a non-negligible population of carbon atoms is associated with intermediate BEs (about 284.5 eV).

The lowest BE component originates from C atoms located on the ripples, which interact weakly with the underlying Ir atoms. Conversely, the highest BE component corresponds to C atoms in the flattest regions of graphene on top of Ir first layer atoms, where the average C–Ir distance is 2.12 Å, indicating a strong interaction with the substrate. The intermediate component is associated with C atoms placed on Ir second layer atoms, where the C–Ir bonding is not as strong as the one with Ir first layer atoms, but not as weak as on ripples.

The strong C–Ir interaction in the flatter region is further evidenced by the Ir $4f_{7/2}$ core level spectrum, which, unlike the case of graphene on Ir(111) [58] where the interaction is dominated by van der Waals forces [57], is significantly affected by graphene growth. Eventually, as in the case of Ir(111), also for this surface the carbon layer consists of a monolayer. This is evidenced by the reduction of the Ir $4f_{7/2}$ core-level signal (see Fig. S2 in the Supplementary Materials), which is very similar in both cases. In fact, for graphene grown on Ir(111) the overall reduction amounts to 37 ± 5 %, which is very close to the value obtained for Ir(311), namely 29 ± 5 %. For Ir(311), the spectrum of the clean surface can be fitted using three components, as shown in Fig. 5(a). The peak at 60.84 eV (Ir_B) is attributed to bulk Ir atoms, while the other two components, shifted by −750 ± 30 meV and −410 ± 30 meV, correspond to first- (Ir_1) and second-layer Ir atoms (Ir_2), respectively [59]. Upon graphene growth, the spectral weight of the lowest BE component is significantly reduced, while its BE remains unchanged (Fig. 5(b)). In contrast, the second-layer Ir component exhibits a slight additional energy shift to −40 meV relative to the clean surface (total BE shift of 450 ± 30 meV relative to Ir_B) and its spectral weight increases. This apparent contradiction—an increase in the spectral weight of second-layer Ir atoms—is explained by the emergence of a new component at a similar BE, as confirmed by the DFT-calculated Ir $4f_{7/2}$ core level histogram in Fig. 5(b).

Indeed, only the first-layer Ir atoms located beneath the ripples retain an almost unchanged Ir $4f_{7/2}$ BE, as shown in the structural model reported in Fig. 5(c), where the color scale associated to the Ir atoms refers to the computed BEs. In contrast, the remaining first-layer Ir atoms, due to their stronger interaction with C atoms, give rise to a new group of Ir atoms with Ir $4f_{7/2}$ BEs that are, however, very close to those of the second-layer atoms, which remain essentially unchanged. As a result, these components are grouped for simplicity into a single fitting component in the spectral analysis.

To further investigate the electronic properties of such a plethora of different interactions, we performed ARPES measurements with the purpose of identifying how the characteristic band structure of graphene is affected either by the ripples (nearly one dimensional and quasi-freestanding) or in the more interacting area (two dimensional with low corrugation). In many cases indeed the coexistence of different structures can be recognized as a simple superposition of spectra coming from the different phases simultaneously illuminated by the photons [60,61]. In Fig. 6(a) spectra acquired at 110 eV photon energy covering more than one surface Brillouin zone (sBZ) show a rich Fermi surface dominated by the Ir states (clean Ir(311) reference data are presented in the Supplementary Material together with comparison at different photon energies in Figs. S3–S5). The characteristic sp-band forming two elongated sharp states along the short side of the sBZ (orange arrows) is clearly visible and can be mistaken for the characteristic Dirac cone of graphene (Fig. 6 (b)). However, considering the energy dispersion of the spectra shown here it is clear that, not only the characteristic triangular shaped constant energy surfaces of graphene π-band are not visible (Fig. 6(c)), but also all the dominating features belong to Ir(311).

The pronounced buckling accounts for the absence of a well-defined π-band in the graphene band structure across various photon energies, consistent with similar observations on Ir(110) and Ru(0001). In accordance with charge density calculation, the detection of sharp surface states associated with Ir(311) is suppressed by the presence of graphene. This contrasts with the case of Ir(111), where the weaker interaction allows these states to remain detectable [63]. One could possibly speculate on the reasons why the one dimensionality of the ripples with higher density of states is not observed in ARPES, however the presence of much stronger intensity coming from the sp-band of the underlying substrate in the same region of k-space thwarts its observation.

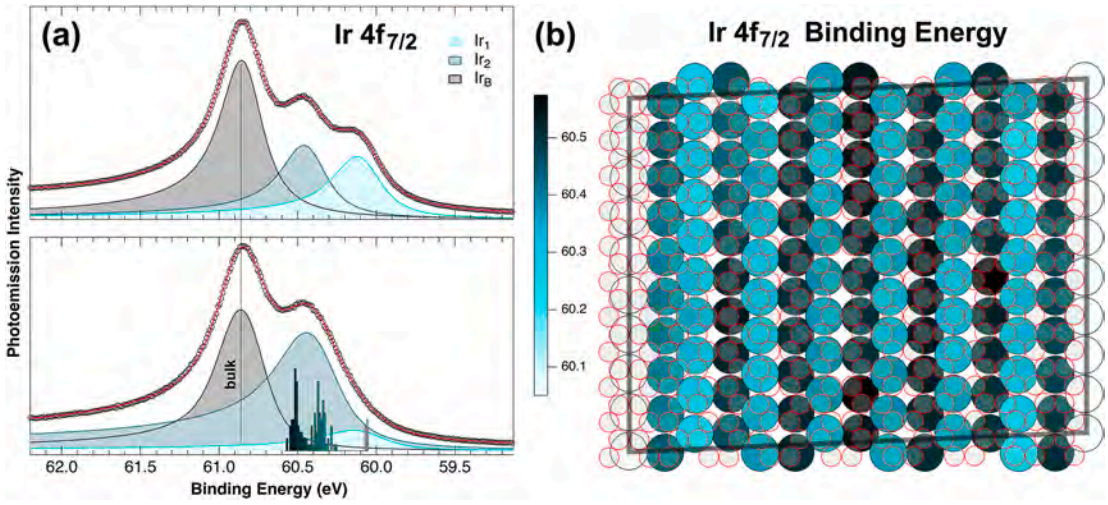

Fig. 5. Ir $4f_{7/2}$ core level spectra and DFT computed Ir core levels distribution. (a) Ir $4f_{7/2}$ core level of clean Ir(311) and (b) graphene covered Ir(311) measured at normal emission and hυ = 200 eV (empty circles) together with the best fit (red solid line). Calculated BE distribution originated by the first- and second-layer Ir atoms of the supercell is reported in panel (b). Different colours are used to identify different components. (c) Structural model of the supercell where the color scale used for non-equivalent Ir atoms reflects the DFT-calculated Ir $4f_{7/2}$ core electron BEs. Carbon atoms are shown as red empty circles. (For interpretation of the references to color in this figure legend, the reader is referred to the Web version of this article.)

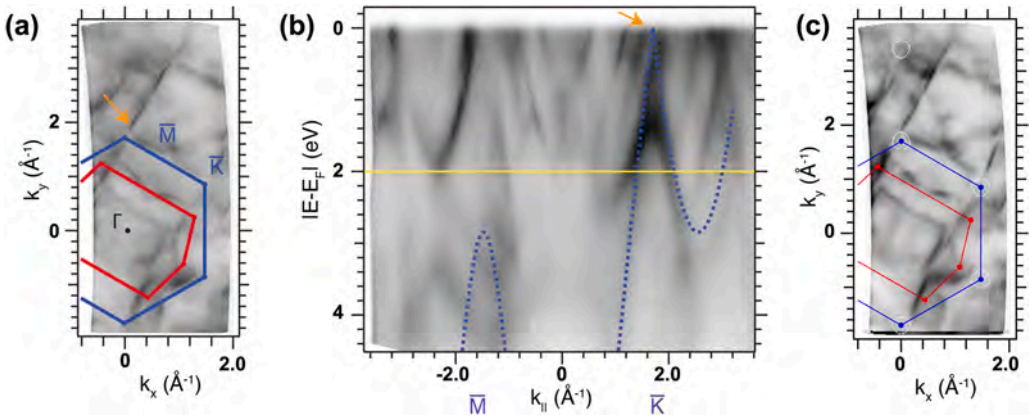

Fig. 6. ARPES measurements on graphene grown on Ir(311). (a) Photoemission intensity at the Fermi level with guide to the eye polygons indicating the Ir(331) sBZ (in red) and the graphene one (in blue). (b) Energy dispersion along the MΓK direction of the graphene BZ. Tight binding calculation for freestanding graphene π-band up to the third nearest neighbours are shown just as a reference guide for the reader with a dashed blue line [62]. (c) Constant energy surface at 2 eV BE (yellow line in (b)) where the typical triangular shaped pockets of the Dirac cones around K are expected to be visible in the free-standing case. (For interpretation of the references to color in this figure legend, the reader is referred to the Web version of this article.)

3.3. Relationship of graphene structural and electronic properties with its curvature

The formation of 1D ripples could be related to the graphene growth temperature and to the different thermal expansion coefficients of Ir and graphene [64], which are known to have opposite signs. The cooling process could induce stress effects in graphene with the consequent formation of strong surface corrugation, as observed in our system. The wrinkling observed in the flatter region of the graphene/Ir(311) system, located between the 1D ripples, is not uncommon, as it closely resembles the structure of graphene on Ir(110) [35]. This 2D corrugation pattern exhibits a buckling amplitude of 0.43 Å along the [2$\overline{3}\overline{3}$] direction, which is very similar to that of graphene on Ir(110) (0.46 Å), and has a periodicity of 8.64 Å. Notably, this corrugation is significantly larger than that of the moirè pattern observed for graphene grown on Ir(111), where the amplitude is only 0.35 Å [57]. We notice that in both graphene/Ir(311) and graphene/Ir(111) systems, the configuration corresponding to the maximum C–Ir separation consists of a carbon hexagon centered directly above a first-layer Ir atom, suggesting that this arrangement minimizes the interaction between graphene and the Ir substrate.

In contrast, the pronounced corrugation observed for the 1D ripples along the [01$\overline{1}$] direction, with a buckling amplitude of 1.29 Å, is exceeded only by the graphene/Ir(100) interface, where the buckling of C atoms is even more pronounced, i.e. 2.1 Å [35]. In this case, the maximum C–Ir separation reaches 4.0 Å, whereas for graphene/Ir(111) the largest C–Ir distance is 3.62 Å, occurring at the peaks of the 2D moiré pattern. For the graphene/Ir(311) system, the maximum C–Ir separation is 3.41 Å, found at the 1D ripples.

The significant variations in C–Ir height are reflected in the C 1s core-electron BEs, where greater C–Ir distances correspond to lower BEs. Additionally, it is important to emphasize that, in the flatter regions of graphene, the interaction with the substrate is strongly influenced by the relative positioning of C atoms with respect to the underlying Ir atoms. C atoms located directly above first-layer Ir atoms exhibit a C 1s core-electron BE that is shifted by up to 0.3 eV toward higher BEs compared to those positioned above second-layer Ir atoms. This shift

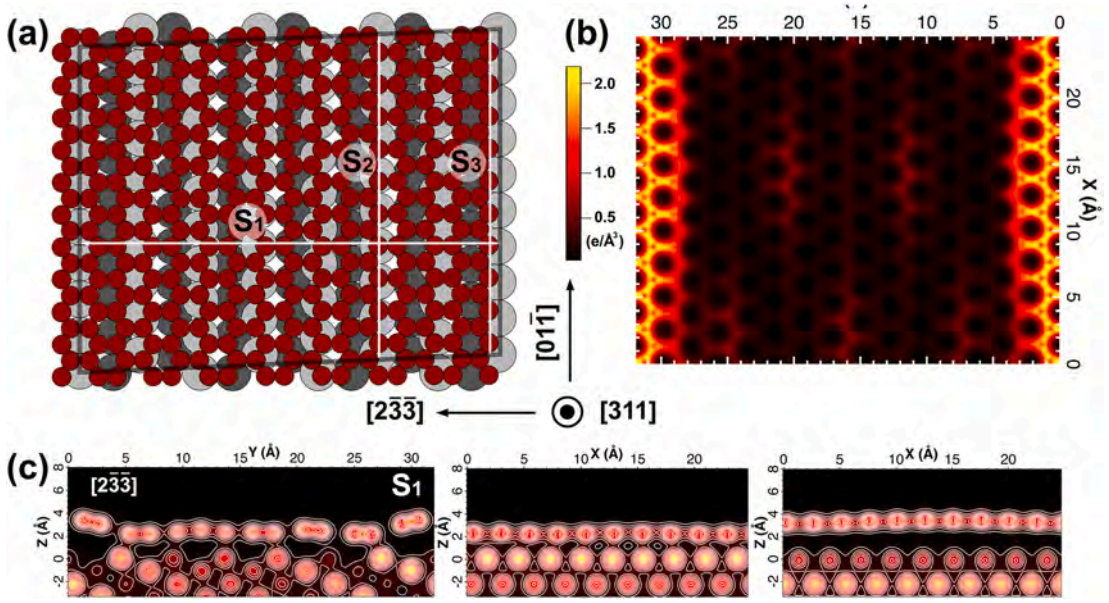

Fig. 7. Computed charge density distribution and charge density iso-surfaces. (a) Supercell with the crystallographic directions of the cuts, shown by segments labelled S_1, S_2 and S_3. (b) Charge density slice along [311] plane. (c) Cuts along [01$\overline{1}$] and [2$\overline{3}\overline{3}$] directions. The direction of the cuts S_1, S_2 and S_3 are reported in panel (a).

indicates minimal charge transfer between these C atoms and the Ir atoms, similar to what is observed in the ripple regions.

To gain deeper insight into the electronic charge redistribution at the graphene/Ir interface, as previously done for graphene on other surfaces [65], we calculated the charge density using a 252 × 320 × 324 grid, ensuring a uniform spacing of 0.1 Å along the [01$\bar{1}$], [2$\bar{3}\bar{3}$], and [311] directions, as illustrated in Fig. 7.

A cut in a plane parallel to the surface, located at a z of 11.44 Å (i.e., 0.2 Å above the ripples) (Fig. 7(b)), highlights the two-dimensional charge localization pattern in the flatter region of graphene, revealing the characteristic bright and dark features observed in STM images. Cuts along non-equivalent planes orthogonal to the surface - specifically along the [2$\bar{3}\bar{3}$] (S_1) and [01$\bar{1}$] (S_2 and S_3) directions - shown in Fig. 7(c) along with charge density iso-surfaces - confirm that the overlap of the charge density between C and Ir atoms is negligible. In contrast, beneath C atoms in the flatter region between the ripples, which are positioned directly above first-layer Ir atoms, there is an increased electron charge localization.

This behavior can be attributed to orbital rehybridization of carbon states toward sp^3 hybridization, as evidenced by both the increased C 1s core-electron BE and the elongation of C–C bond lengths, which experience tensile strain (see Fig. 8). Strain is defined as the percentage variation of the average C–C distance between nearest neighbours atoms with respect to the value of unstrained graphene, i.e. 1.42 Å. Our findings are in good agreement with those of Haerle et al. [66], who reported that the C 1s core-electron BE for sp^3-hybridized carbon is approximately 0.8 eV higher than that of sp^2 carbon atoms. This shift closely matches the difference we observe between the weakly and strongly interacting C 1s components in the graphene/Ir(311) system, further supporting the presence of carbon orbital rehybridization.

In contrast to the flatter regions, graphene lattice in the ripple regions experiences compressive strain, as shown in Fig. 8. This effect can have significant consequences on the local reactivity of graphene. As shown by McKay et al. [67] indeed the compressive strain in graphene substantially reduces the dissociation barrier of H_2. More broadly, variations in graphene corrugation have been linked to changes in its chemical reactivity: the greater the corrugation, the higher the chemisorption energy, such as in the case of H_2 (less than −1.5 eV/H_2 for highly curved graphene) [68], which is known to be only 50 meV for free-standing graphene [69].

A widely used parameter to quantify graphene corrugation is the ratio between the ripple height h and its diameter d (or radius R), expressed as a percentage. In our system, which exhibits both one- and two-dimensional corrugations, the 2D periodic wave pattern results in a curvature of 7 % (h/R ratio of 0.14), whereas the 1D periodic ripples reach a corrugation value of 11 %. For comparison, the hills of the moiré pattern of graphene on Ru(0001) and Ir(111) exhibit local curvatures of approximately 7 % and 1 %, respectively (see Fig. S6 in the Supplementary Material).

Notably, our values are comparable to the threshold reported by Boukhvalov (h/R = 0.07), above which H_2 chemisorption becomes energetically favorable [68]. This observation is further supported by recent DFT calculations and Raman spectroscopy data: for curvatures exceeding 10 % (h/d ratio >0.10), the energy barrier for H_2 dissociation drops below 1 eV, significantly lower than the 3-eV barrier reported for flat graphene [70,71].

Beyond hydrogen dissociation, graphene rippling has been shown to enhance catalytic activity in various contexts. For example, aryl radicals selectively adsorb and react with highly corrugated regions of graphene [72], and functionalization with 4-nitrobenzenediazonium tetrafluoroborate becomes energetically more favorable as out-of-plane distortions in carbon lattice increase [73]. Furthermore, curved graphene has been reported to improve the reactivity of single-atom catalysts in ammonia synthesis [74].

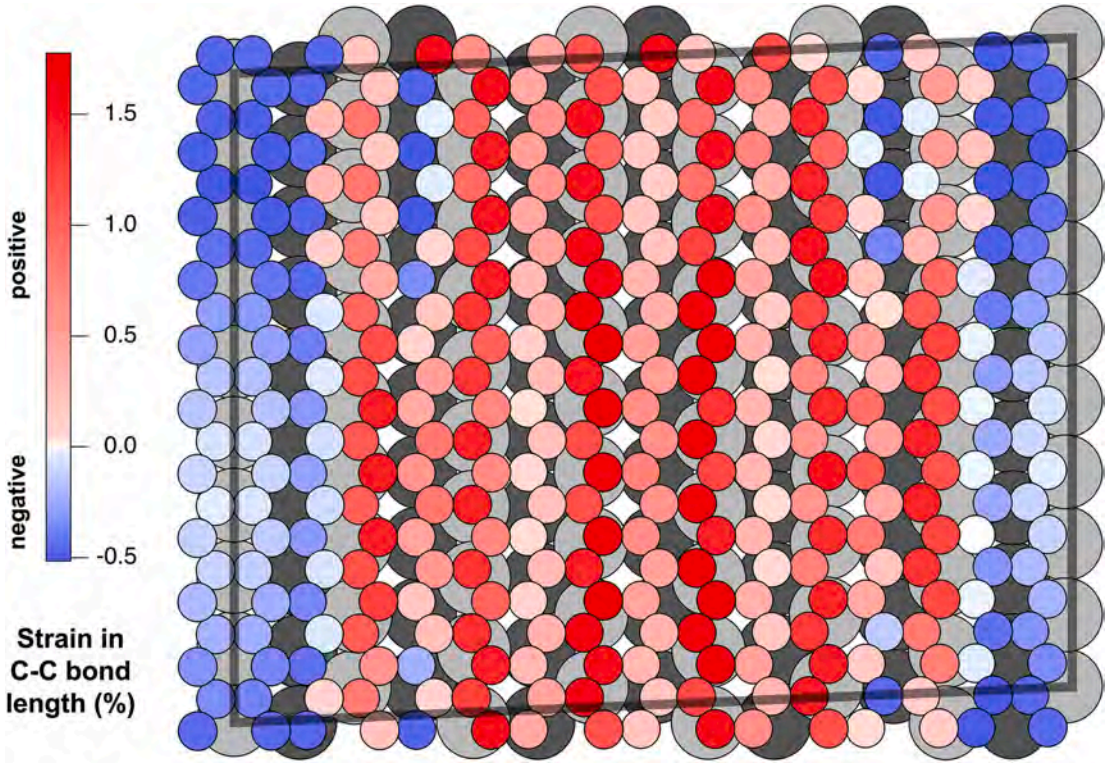

Fig. 8. Colour map of average strain in graphene. Strain is defined as the percentual average variation in the C–C bond length between nearest neighbours atoms with respect to the value of 1.42 Å. The color scale of the plot ranges from positive strain in red to negative strain in blue. (For interpretation of the references to color in this figure legend, the reader is referred to the Web version of this article.)

4. Conclusions

In this work, we have demonstrated that the growth of graphene on Ir (311) leads to the formation of a monolayer exhibiting a unique coexistence of corrugations with different physical dimensionalities—specifically, both one-dimensional and two-dimensional periodic modulations—combined with a pronounced degree of curvature. This structural configuration results in a highly buckled graphene sheet, distinct from what is typically observed on low-index metal surfaces.

The ability to engineer two distinct periodic curvatures with substantial corrugation amplitudes, as shown in our graphene/metal model system, opens new opportunities for tailoring the chemical reactivity of graphene. Such a double-curvature configuration could endow graphene with bifunctional catalytic properties, where different regions may selectively interact with distinct chemical species. Moreover, the enhanced curvature, with local mechanical strain [75], could enable graphene to act as an efficient, lightweight material for temperature-controlled hydrogen adsorption and release. Besides its relevance for chemical reactivity, curved graphene is known to induce electron-hole asymmetric spin splitting and varied energy-level behaviours under magnetic fields [76]. Curvature-induced spin-orbit coupling is also recognized to design materials with valley-contrasting spin-orbit interactions, thus providing strategies for tailoring electronic properties through curvature manipulation [77].

Finally, our findings suggest that the synthesis of corrugated graphene with tunable curvature profiles is not necessarily limited to Ir (311), but could, in principle, be extended to other anisotropic and potentially more cost-effective substrates, such as copper and nickel. This approach may pave the way for scalable strategies to fabricate chemically versatile graphene-based systems with promising applications in catalysis, electrochemistry, hydrogen storage, and offering pathways for designing advanced materials in spintronics and related fields.

CRediT authorship contribution statement

Deborah Perco: Writing – review & editing, Writing – original draft, Investigation, Formal analysis, Data curation. **Monica Pozzo:** Writing – review & editing, Formal analysis, Data curation. **Marco Bianchi:** Writing – review & editing, Investigation, Formal analysis, Data curation. **Paolo Lacovig:** Writing – review & editing, Investigation. **Francesco Sammartino:** Writing – review & editing, Investigation. **Philip Hofmann:** Writing – review & editing, Validation, Funding acquisition. **Silvano Lizzit:** Writing – review & editing, Validation, Investigation. **Dario Alfè:** Writing – review & editing, Validation, Supervision, Funding acquisition, Formal analysis, Data curation. **Alessandro Baraldi:** Writing – review & editing, Writing – original draft, Supervision, Investigation, Funding acquisition, Conceptualization.

Declaration of competing interest

The authors declare the following financial interests/personal relationships which may be considered as potential competing interests: Alessandro Baraldi and Dario Alfè report financial support was provided by Ministero dell'Università e della Ricerca. Philip Hofmann reports financial support was provided by Independent Research Fund Denmark. If there are other authors, they declare that they have no known competing financial interests or personal relationships that could have appeared to influence the work reported in this paper.

5. Acknowledgments

A.B. gratefully acknowledges the financial support from the National Quantum Science and Technology Institute (PNRR MUR projectPE0000023-NQSTI). A.B. and D.A. acknowledge MUR for the support of the PRIN Project no. 20222FXZ33 entitled "Materials modelling for energy storage applications". This work used the ARCHER2 UK National Supercomputing Service (https://www.archer2.ac.uk). Ph. H. acknowledges the financial support from Independent Research Fund Denmark (Grant No. 1026-00089B). We acknowledge Elettra-Sincrotrone Trieste for providing access to its synchrotron radiation facilities and for financial support.

Appendix A. Supplementary data

Supplementary data to this article can be found online at https://doi.org/10.1016/j.carbon.2025.120934.

References

[1] K.S. Novoselov, V.I. Fal'ko, L. Colombo, P.R. Gellert, M.G. Schwab, K. Kim, A roadmap for graphene, Nature 490 (2012) 192, https://doi.org/10.1038/nature11458.
[2] P. Avouris, Z. Chen, V. Perebeinos, Carbon-based electronics, Nat. Nanotech. 2 (2007) 605–615, https://doi.org/10.1038/nnano.2007.300.
[3] A.K. Geim, K.S. Novoselov, The rise of graphene, Nat. Mater 6 (2007) 183–191, https://doi.org/10.1038/nmat1849.
[4] C.N.R. Rao, A.K. Sood, K.S. Subrahmanyam, A. Govindaraj, Graphene: the new two-dimensional nanomaterial, Angew. Chem. Int. Edit. 48 (2009) 7752–7777, https://doi.org/10.1002/anie.200901678.
[5] B.F. Machado, P. Serp, Graphene-based materials for catalysis, Catal. Sci. Technol. 2 (2012) 54–75, https://doi.org/10.1039/C1CY00361E.
[6] X. Fan, G. Zhang, F. Zhang, Multiple roles of graphene in heterogeneous catalysis, Chem. Rev. Soc. 44 (2015) 3023–3035, https://doi.org/10.1039/C5CS00094G.
[7] J.J. Navarro, M. Pisarra, B. Nieto-Ortega, J. Villalva, C.G. Ayani, C. Diaz, F. Calleja, R. Miranda, F. Martin, E.M. Perez, A.L. Vazquez de Parga, Graphene catalyzes the reversible formation of a C-C bond between two molecules, Sci. Adv. 4 (2018) 12, https://doi.org/10.1126/sciadv.aau9366.
[8] J. Tu, M. Yan, Enhancing the chemical reactivity of graphene through substrate engineering, Small (2024) 2408116, https://doi.org/10.1002/smll.202408116.
[9] Y. Qu, Y. Ke, Y. Shao, W. Chen, C.T. Kwok, X. Shi, H. Pan, Effect of curvature on the hydrogen evolution reaction of graphene, J. Phys. Chem. C 122 (2018) 25331–25338, https://doi.org/10.1021/acs.jpcc.8b06750.
[10] M. Zhou, A. Zhang, Z. Dai, Y.P. Feng, C. Zhang, Strain-enhanced stabilization and catalytic activity of metal nanoclusters on graphene, J. Phys. Chem. C 114 (2010) 16541–16546, https://doi.org/10.1021/jp105368j.
[11] A. Ganyecz, M. Kallay, Oxygen reduction reaction on N-Doped graphene: effect of positions and scaling relations of adsorption energies, J. Phys. Chem. C 125 (2021) 8551–8561, https://doi.org/10.1021/acs.jpcc.0c11340.
[12] K. Parvez, S. Yang, Y. Hernandez, A. Winter, A. Turchanin, X. Feng, K. Müllen, Nitrogen-doped graphene and its iron-based composite as efficient electrocatalysts for oxygen reduction reaction, ACS Nano 6 (2012) 9541–9550, https://doi.org/10.1021/nn302674k.
[13] Z.-S. Wu, K. Parvez, A. Winter, H. Vieker, X. Liu, S. Han, A. Turchanin, X. Feng, K. Müllen, Layer-by-Layer assembled heteroatom-doped graphene films with ultrahigh volumetric capacitance and rate capability for micro-supercapacitors, Adv. Mater. 26 (2014) 4552–4558, https://doi.org/10.1002/adma.201401228.
[14] J. Wintterlin, M.-L. Bocquet, Graphene on metal surfaces, Surf. Sci. 603 (2009) 1841–1852, https://doi.org/10.1016/j.susc.2008.08.037.
[15] C. Berger, Z. Song, X. Li, X. Wu, N. Brown, C. Naud, D. Mayou, T. Li, J. Hass, A. N. Marchenkov, E.H. Conrad, Ph N. First, W.A. De Heer, Electronic confinement and coherence in patterned epitaxial graphene, Science 312 (2006) 1191–1196, https://doi.org/10.1126/science.1125925.
[16] S. Lou, X. Ma, Z. Wang, W. Wang, L. Song, X. Sun, Y. Ding, W.-J. Yin, W. Yang, J. Tan, X. Sun, Z. Liu, Interfacial coupling induced discrete orientation of epitaxial graphene on high-index Cu substrates, Adv. Funct. Mater. 35 (2024) 2415972, https://doi.org/10.1002/adfm.202415972.
[17] O.J. Burton, Z. Winter, K. Watanabe, T. Taniguchi, B. Beschoten, C. Stampfer, S. Hofmann, Putting high-index Cu on the map for high-yield, dry-transferred CVD graphene, ACS Nano 17 (2023) 1229–1238, https://doi.org/10.1021/acsnano.2c09253.
[18] A.B. Preobrajenski, M.L. Ng, A.S. Vinogradov, N. Mårtensson, Controlling graphene corrugation on lattice-mismatched substrates, Phys. Rev. B 78 (2008) 073401, https://doi.org/10.1103/PhysRevB.78.073401.
[19] P. Sutter, J.T. Sadowski, E. Sutter, Graphene on Pt(111): growth and substrate interaction, Phys. Rev. B 80 (2009) 245411, https://doi.org/10.1103/PhysRevB.80.245411.
[20] R. Larciprete, S. Ulstrup, P. Lacovig, M. Dalmiglio, M. Bianchi, F. Mazzola, L. Hornekær, F. Orlando, A. Baraldi, P. Hofmann, S. Lizzit, Oxygen switching of the epitaxial graphene–metal interaction, ACS Nano 6 (2012) 9551–9558, https://doi.org/10.1021/nn302729j.
[21] Y. Ma, E. Travaglia, H. Bana, L. Bignardi, P. Lacovig, S. Lizzit, M. Batzill, Periodic modulation of graphene by a 2D-FeO/Ir(111) moirè interlayer, J. Phys. Chem. C 121 (2017) 2762–2770, https://doi.org/10.1021/acs.jpcc.6b11112.
[22] E. Miniussi, M. Pozzo, A. Baraldi, E. Vesselli, R.R. Zhan, C. Comelli, T.O. Mentes, M.A. Nino, A. Locatelli, S. Lizzit, D. Alfè, Thermal stability of corrugated epitaxial graphene grown on Re(0001), Phys. Rev. Lett. 106 (2011) 216101, https://doi.org/10.1103/PhysRevLett.106.216101.

[23] E.N. Voloshina, Y.S. Dedkov, S. Torbrugge, A. Thissen, M. Fonin, Graphene on Rh (111): STM and AFM studies, Appl. Phys. Lett. 100 (2012) 241606, https://doi.org/10.1063/1.4729549.

[24] D. Martoccia, P.R. Willmott, T. Brugger, M. Bjorck, S. Günther, C.M. Schleputz, A. Cervellino, S.A. Pauli, B.D. Patterson, S. Marchini, J. Wintterlin, W. Moritz, T. Greber, Graphene on Ru(0001): a 25 ×25 supercell, Phys. Rev. Lett. 101 (2008) 126102, https://doi.org/10.1103/PhysRevLett.101.126102.

[25] D. Alfè, M. Pozzo, E. Miniussi, S. Günther, P. Lacovig, S. Lizzit, R. Larciprete, B. Santos Burgos, T.O. Mentes, A. Locatelli, A. Baraldi, Fine tuning of graphene-metal adhesion by surface alloying, Sci. Rep. 3 (2013) 2430, https://doi.org/10.1038/srep02430.

[26] L.Z. Zhang, S.X. Du, T. Sun, L. Huang, L. Meng, W.Y. Xu, L.D. Pan, Y. Pan, Y. L. Wang, W.A. Hofer, H.-J. Gao, Growth mechanism of metal clusters on a Graphene/Ru(0001) template, Adv. Mater. Interfaces 1 (2014) 3, https://doi.org/10.1002/admi.201300104.

[27] M.D. Jiménez-Sánchez, C. Romero-Muniz, P. Pou, R. Perez, J.M. Gomez-Rodriguez, Graphene on Rh(111): a template for growing ordered arrays of metal nanoparticles with different periodicities, Carbon 173 (2021) 1073–1081, https://doi.org/10.1016/j.carbon.2020.11.086.

[28] M. Scardamaglia, G. Forte, S. Lizzit, A. Baraldi, P. Lacovig, R. Larciprete, C. Mariani, M.G. Betti, Metal-phthalocyanine array on the moiré pattern of a graphene sheet, J. Nanopart. Res. 13 (2011) 6013–6020, https://doi.org/10.1007/s11051-011-0384-1.

[29] M. Bazarnik, J. Brede, R. Decker, R. Wiesendanger, Tailoring molecular self-assembly of magnetic phthalocyanine molecules on Fe- and Co-Intercalated graphene, ACS Nano 7 (2013) 11341–11349, https://doi.org/10.1021/nn405172q.

[30] Z. Novotny, F.P. Netzer, Z. Dohnalek, Cerium oxide nanoclusters on Graphene/Ru (0001): intercalation of oxygen via spillover, ACS Nano 9 (2015) 8617–8626, https://doi.org/10.1021/acsnano.5b03987.

[31] A. Cavallin, M. Pozzo, C. Africh, A. Baraldi, E. Vesselli, C. Dri, G. Comelli, R. Larciprete, P. Lacovig, S. Lizzit, D. Alfè, Local electronic structure and density of edge and facet atoms at Rh nanoclusters self-assembled on a graphene template, ACS Nano 6 (2012) 3034–3043, https://doi.org/10.1021/nn300651s.

[32] C. Diaz, F. Calleja, A.L. Vázquez de Parga, F. Martín, Graphene grown on transition metal substrates: versatile templates for organic molecules with new properties and structures, Surf. Sci. Rep. 77 (2022) 100575, https://doi.org/10.1016/j.surfrep.2022.100575.

[33] Y. Du, D. Yi, X. Wang, Carbon-rehybridization-induced templated growth of metal nanoclusters on graphene moiré patterns, Carbon 192 (2022) 295–300, https://doi.org/10.1016/j.carbon.2022.03.002.

[34] Y. Li, X. Liu, C. Chen, J. Duchamp, R. Huang, T.-F. Chung, M. Young, T. Chalal, Y. P. Chen, J.R. Heflin, H.C. Dorn, C. Tao, Differences in self-assembly of spherical C_{60} and planar PTCDA on rippled graphene surfaces, Carbon 145 (2019) 549–555, https://doi.org/10.1016/j.carbon.2019.01.070.

[35] A. Locatelli, G. Zamborlini, T.O. Mentes, Growth of single and multi-layer graphene on Ir(100), Carbon 74 (2014) 237–248, https://doi.org/10.1016/j.carbon.2014.03.028.

[36] M. Imam, N. Stojić, N. Binggeli, First-principle investigation of a rippled graphene phase on Ir(001): the close link between periodicity, stability, and binding, J. Phys. Chem. C 118 (2014) 9514–9523, https://doi.org/10.1021/jp5010727.

[37] A. Locatelli, C. Wang, C. Africh, N. Stojic, T.O. Mentes, G. Comelli, N. Binggeli, Temperature-driven reversible rippling and bonding of a graphene superlattice, ACS Nano 7 (2013) 8, https://doi.org/10.1021/nn402178u.

[38] F. Presel, N. Jabeen, M. Pozzo, D. Curcio, L. Omiciuolo, P. Lacovig, S. Lizzit, D. Alfè, A. Baraldi, Unravelling the roles of surface chemical composition and geometry for the graphene-metal interaction through C1s core-level spectroscopy, Carbon 93 (2015) 187, https://doi.org/10.1016/j.carbon.2015.05.041.

[39] L. Bignardi, P. Lacovig, R. Larciprete, D. Alfè, S. Lizzit, A. Baraldi, 2D materials at surfaces through synchrotron-based core-level photoelectron spectroscopy, Surf. Sci. Rep. 78 (2023) 100586, https://doi.org/10.1016/j.surfrep.2023.100586.

[40] C. Lin, X. Huang, F. Ke, C. Jin, N. Tong, X. Yin, L. Gan, X. Guo, R. Zhao, W. Yang, E. Wang, Z. Hu, Quasi-one-dimensional graphene superlattices formed on high-index surfaces, Phys. Rev. B 89 (2014) 085416, https://doi.org/10.1103/PhysRevB.89.085416.

[41] N.A. Vinogradov, A.A. Zakharov, A.A. Kocevski, J. Rusz, K.A. Simonov, O. Eriksson, A. Mikkelsen, E. Lundgren, A.S. Vinogradov, N. Martensson, A. B. Preobrajenski, Formation and structure of graphene waves on Fe(110), Phys. Rev. Lett. 109 (2012) 026101, https://doi.org/10.1103/PhysRevLett.109.026101.

[42] I.S. Rakic, M. Kralj, W. Jolie, P. Lazic, W. Sun, J. Avila, M.C. Asensio, F. Craes, V. M. Trontl, C. Busse, P. Pervan, Step-induced faceting and related electronic effects for graphene on Ir(332), Carbon 110 (2016) 267–277, https://doi.org/10.1016/j.carbon.2016.09.024.

[43] A. Celis, M.N. Nair, M. Sicot, F. Nicolas, S. Kubsky, A. Taleb-Ibrahimi, D. Malterre, A. Tejeda, Growth, morphology and electronic properties of epitaxial graphene on vicinal Ir(332) surface, Nanotechnol 31 (2020) 285601, https://doi.org/10.1088/1361-6528/ab866a.

[44] S. Kraus, F. Huttmann, J. Fischer, T. Knispel, K. Bischof, A. Herman, M. Bianchi, R. M. Stan, A.J. Holt, V. Caciuc, S. Tsukamoto, H. Wende, P. Hofmann, N. Atodiresei, T. Michely, Single-crystal graphene on Ir(110), Phys. Rev. B 105 (2022) 165405, https://doi.org/10.1103/PhysRevB.105.165405.

[45] P.V. Antonov, P. Restuccia, M.C. Righi, J.W.M. Frenken, Attractive curves: the role of deformations in adhesion and friction on graphene, Nanoscale Adv. 4 (2022) 4175, https://doi.org/10.1039/D2NA00283C.

[46] X. Gao, Y. Wang, X. Liu, T.-L. Chan, S. Irle, Y. Zhao, S.B. Zhang, Regioselectivity control of graphene functionalization by ripples, Phys. Chem. Chem. Phys. 13 (2011) 19449–19453, https://doi.org/10.1039/C1CP22491C.

[47] A. Politano, G. Chiarello, Periodically rippled graphene on Ru(0001): a template for site-selective adsorption of hydrogen dimers via water splitting and hydrogen-spillover at room temperature, Carbon 61 (2013) 412–417, https://doi.org/10.1016/j.carbon.2013.05.025.

[48] S.V. Hoffmann, C. Søndergaard, C. Schultz, Z. Li, Ph Hofmann, An undulator-based spherical grating monochromator beamline for angle-resolved photoemission spectroscopy, Nucl. Instrum. Meth. A 532 (2004) 441, https://doi.org/10.1016/j.nima.2004.01.039.

[49] G. Kresse, J. Furthmüller, Efficient iterative schemes for ab initio total-energy calculations using a plane-wave basis set, Phys. Rev. B 54 (1996) 11169–11186, https://doi.org/10.1103/PhysRevB.54.11169.

[50] I. Hamada, van der Waals density functional made accurate, Phys. Rev. B 89 (2014) 121103, https://doi.org/10.1103/PhysRevB.89.121103.

[51] P.E. Blöchl, Projector augmented-wave method, Phys. Rev. B 50 (1994) 17953–17979, https://doi.org/10.1103/PhysRevB.50.17953.

[52] G. Kresse, D. Joubert, From ultrasoft pseudopotentials to the projector augmented-wave method, Phys. Rev. B 59 (1999) 1758–1775, https://doi.org/10.1103/PhysRevB.59.1758.

[53] J.P. Perdew, K. Burke, M. Ernzerhof, Generalized gradient approximation made simple, Phys. Rev. Lett. 77 (1996) 3865–3868, https://doi.org/10.1103/PhysRevLett.77.3865.

[54] H. Orita, Y. Inada, DFT investigation of CO adsorption on Pt(211) and Pt(311) surfaces from low to high coverage, J. Phys. Chem. B 109 (2005) 22469–22475, https://doi.org/10.1021/jp052583a.

[55] H. Tetlow, J.P. de Boer, I.J. Ford, D.D. Vvedensky, D. Curcio, L. Omiciuolo, S. Lizzit, A. Baraldi, L. Kantorovich, Ethylene decomposition on Ir(111): initial path to graphene formation, Phys. Chem. Chem. Phys. 18 (2016) 27897–27909, https://doi.org/10.1039/C6CP03638D.

[56] P. Prochazka, J. Cechal, ProLEED studio: software for modeling low-energy electron diffraction patterns, J. Appl. Cryst. 57 (2024) 187–193, https://doi.org/10.1107/S1600576723010312.

[57] C. Busse, P. Lazic, R. Djemour, J. Coraux, T. Gerber, N. Atodiresei, V. Caciuc, R. Brako, A.T. N'Diaye, S. Blugel, J. Zegenhagen, T. Michely, Graphene on Ir(111): physisorption with chemical modulation, Phys. Rev. Lett. 107 (2011) 036101, https://doi.org/10.1103/PhysRevLett.107.036101.

[58] P. Lacovig, M. Pozzo, D. Alfè, P. Vilmercati, A. Baraldi, S. Lizzit, Growth of dome-shaped carbon nanoislands on Ir(111): the intermediate between carbidic clusters and quasi-free-standing graphene, Phys. Rev. Lett. 103 (2009) 179904, https://doi.org/10.1103/PhysRevLett.103.166101.

[59] D. Perco, M. Pozzo, A. Berti, P. Lacovig, M. Bianchi, S. Lizzit, D. Alfè, A. Baraldi, A high-resolution core level spectroscopy study of ir: from flat to reconstructed and stepped surfaces, Appl. Surf. Sci. 702 (2025) 163294–163303, https://doi.org/10.1016/j.apsusc.2025.163294.

[60] M. Bianchi, E.D.L. Rienks, S. Lizzit, A. Baraldi, R. Balog, L. Hornekær, Ph Hofmann, Electron-phonon coupling in potassium-doped graphene: angle-resolved photoemission spectroscopy, Phys. Rev. B 81 (2010) 041403, https://doi.org/10.1103/PhysRevB.81.041403 (R).

[61] C. Struzzi, C.S. Praveen, M. Scardamaglia, N.I. Verbitskiy, A.V. Fedorov, M. Weini, M. Schreck, A. Grüneis, S. Piccinin, S. Fabris, L. Petaccia, Controlled thermodynamics for tunable electron doping of graphene on Ir(111), Phys. Rev. B 94 (2016) 085427, https://doi.org/10.1103/PhysRevB.94.085427.

[62] A. Bostwick, T. Ohta, T. Seyller, K. Horn, E. Rotenberg, Quasiparticle dynamics in graphene, Nat. Phys. 3 (2007) 36–40, https://doi.org/10.1038/nphys477.

[63] A. Varykhalov, D. Marchenko, M.R. Scholz, E.D.L. Rienks, T.K. Kim, G. Bihlmayer, J. Sanchez-Barriga, O. Rader, Ir(111) surface state with giant rashba splitting persists under graphene in air, Phys. Rev. Lett. 108 (2012) 066804, https://doi.org/10.1103/PhysRevLett.108.066804.

[64] M. Pozzo, D. Alfè, P. Lacovig, P. Hofmann, S. Lizzit, A. Baraldi, Thermal expansion of supported and freestanding graphene: lattice constant versus interatomic distance, Phys. Rev. Lett. 106 (2011) 135501, https://doi.org/10.1103/PhysRevLett.106.135501.

[65] L. Adamska, Y. Lin, A.J. Ross, M. Batzill, I.I. Oleynik, Atomic and electronic structure of simple metal/graphene and complex metal/graphene/metal interfaces, Phys. Rev. B 85 (2012) 195443, https://doi.org/10.1103/PhysRevB.85.195443.

[66] R. Haerle, E. Riedo, A. Pasquarello, A. Baldereschi, sp2/sp3 hybridization ratio in amorphous carbon C 1s core-level shifts: X-ray photoelectron spectroscopy and first-principles calculation, Phys. Rev. B 65 (2001) 045101, https://doi.org/10.1103/PhysRevB.65.045101.

[67] H. McKay, D.J. Wales, S.J. Jenkins, J.A. Verges, P.L. de Andres, Hydrogen on graphene under stress: molecular dissociation and gap opening, Phys. Rev. B 81 (2010) 075425, https://doi.org/10.1103/PhysRevB.81.075425.

[68] D.W. Boukhvalov, M. Katsnelson, Enhancement of chemical activity in corrugated graphene, J. Phys. Chem. C 113 (2009) 14176–14178, https://doi.org/10.1021/jp905702e.

[69] Y.S. Al-Hamdani, D. Alfè, A. Michaelides, How strongly do hydrogen and water molecules stick to carbon nanomaterials? J. Chem. Phys. 146 (2017) 094701 https://doi.org/10.1063/1.4977180.

[70] P.Z. Sun, W.Q. Xiong, A. Bera, I. Timokhin, Z.F. Wu, A. Mishchenko, M.C. Sellers, B.L. Liu, H.M. Cheng, E. Janzen, J.H. Edgar, I.V. Grigorieva, S.J. Yuan, A.K. Geim, Unexpected catalytic activity of nanorippled graphene, Proc. Natl. Acad. Sci. USA. 120 (2023) 12, https://doi.org/10.1073/pnas.2300481120.

[71] W. Xiong, W. Zhou, P. Sun, S. Yuan, Enhanced hydrogen-gas permeation through rippled graphene, Phys. Rev. B 108 (2023) 045408, https://doi.org/10.1103/PhysRevB.108.045408.
[72] Q. Wu, Y. Wu, Y. Hao, J. Geng, M. Charlton, S. Chen, Y. Ren, H. Ji, H. Li, D. W. Boukhvalov, R.D. Piner, C.W. Bielawski, R.S. Ruoff, Selective surface functionalization at regions of high local curvature in graphene, Chem. Comm. 49 (2013) 677, https://doi.org/10.1039/C2CC36747E.
[73] N. Hawthorne, S. Banerjee, Q. Moore, A.M. Rappe, J.D. Batteas, Studies of the reactivity of graphene driven by mechanical distortions, J. Phys. Chem. C 126 (2022) 17569–17578, https://doi.org/10.1021/acs.jpcc.2c05261.
[74] D. Liu, H. Ai, W.T. Lou, F. Li, K.H. Lo, S. Wang, H. Pan, Substrate strain engineering: an efficient strategy to enhance the catalytic activity of SACs on waved graphene for e-NRR, Sustain. Energy Fuels 4 (2020) 3773, https://doi.org/10.1039/D0SE00518E.
[75] M. Bisset, S. Konabe, S. Okada, M. Tsuji, H. Ago, Enhanced chemical reactivity of graphene induced by mechanical strain, ACS Nano 7 (2013) 10335–10343, https://doi.org/10.1021/nn404746h.
[76] J.-S. Jeong, H.-W. Lee, Curvature-enhanced spin-orbit coupling in a carbon nanotube, Phys. Rev. B 80 (2009) 075409, https://doi.org/10.1103/PhysRevB.80.075409.
[77] P. Gentile, M. Cuoco, O.M. Volkov, Z.-J. Ying, I.J. Vera-Marun, D. Makarov, C. Ortix, Electronic materials with nanoscale curved geometries, Nat. Electron. 5 (2022) 551–563, https://doi.org/10.1038/s41928-022-00820-z.